ACS Catalysis

pubs.acs.org/acscatalysis Research Article

Immobilization of "Capping Arene" Cobalt(II) Complexes on Ordered Mesoporous Carbon for Electrocatalytic Water Oxidation

Chang Liu,[#] Ana M. Geer,[#] Christopher Webber, Charles B. Musgrave III, Shunyan Gu, Grayson Johnson, Diane A. Dickie, Sonia Chabbra, Alexander Schnegg, Hua Zhou, Cheng-Jun Sun, Sooyeon Hwang, William A. Goddard III,* Sen Zhang,* and T. Brent Gunnoe*

Cite This: *ACS Catal.* 2021, 11, 15068−15082 Read Online

ACCESS | Metrics & More | Article Recommendations | Supporting Information

ABSTRACT: We report the synthesis, characterization, and electrocatalytic water oxidation activity of two cobalt complexes, (6-FP)Co$(NO_3)_2$ (**1**) (6-FP = 8,8′-(1,2-phenylene)diquinoline) and (5-FP)Co$(NO_3)_2$ (**2**) (5-FP = 1,2-bis(*N*-7-azaindolyl)-benzene), containing "capping arene" bidentate ligands with nitrogen atom donors. The cobalt complexes **1** and **2** were supported on ordered mesoporous carbon (OMC) by $\pi-\pi$ stacking, resulting in heterogenized cobalt materials **6-FP-Co-OMC-1** and **5-FP-Co-OMC-2**, respectively, and studied for electrocatalytic water oxidation. We find that **6-FP-Co-OMC-1** exhibits an overpotential of 355 mV for a current density of 10 mA cm^{-2} and a turnover frequency (TOF) of ∼0.53 s^{-1} at an overpotential of 400 mV at pH 14. **6-FP-Co-OMC-1** exhibits activity that is ∼1.6 times that of **5-FP-Co-OMC-2**, which gives a TOF of 0.32 s^{-1} at 400 mV overpotential. The structural stability of the single-atom Co site was demonstrated for **6-FP-Co-OMC-1** using X-ray absorption spectroscopy for the molecular complex supported on OMC, but slow degradation in catalyst activity can be attributed to eventual formation of Co oxide clusters. DFT computations of electrocatalytic water oxidation using the molecular complexes as models provide a description of the catalytic mechanism. These studies reveal that the mechanism for O−O bond formation involves an intermediate Co^{IV} oxo complex that undergoes an intramolecular reductive O−O coupling to form a Co^{II}−OOH species. Further, the calculations predict that the molecular 6-FP-Co structure is more active for electrocatalytic water oxidation than 5-FP-Co, which is consistent with experimental studies of **6-FP-Co-OMC-1** and **5-FP-Co-OMC-2**, highlighting the possibility that the ligand structure influences the catalytic activity of the supported molecular catalysts.

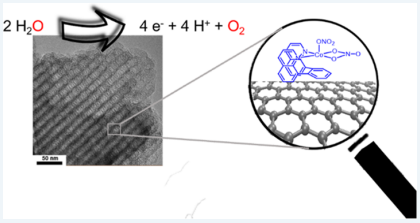

KEYWORDS: *cobalt, ordered mesoporous carbon, supported catalyst, electrocatalysis, water oxidation, conducting carbon*

INTRODUCTION

Artificial photosynthesis for water splitting using renewable energy-based alternatives to fossil fuels offers potential to implement clean energy processes.[1−5] Improvement of the efficiency and stability of the electrocatalysts for the anodic reaction, the oxygen evolution reaction (OER), is imperative for the development of large-scale water splitting.[6,7] Homogeneous molecular electrocatalysts for water oxidation have been extensively investigated, and the tunable structures and well-defined active sites have led to detailed mechanistic understanding as well as the advancement of more active and longer-lived catalysts.[8−13] There has been interest in first-row transition metal complexes due to the advantages of earth abundance and low cost compared to their noble metal counterparts.[14−20]

In particular, cobalt-based molecular catalysts for electrochemical water oxidation have been studied due to their high catalytic activity.[21−27] Given the lability of Co^{II} ligand bonds and the propensity for oxidative degradation,[28] the formation of CoO_x using molecular Co complexes under oxidizing conditions is common.[29−32] Multidentate chelating ligands can provide stability to the metal center to help mitigate degradation under oxidative conditions. For example, Berlinguette and co-workers reported a pentadentate polypyridine Co^{II} complex (**a**, Scheme 1) that catalyzes electrochemical water oxidation under basic conditions.[33,34] At pH > 10.2, the formation of CoO_x was observed; however, the catalyst was proposed to remain homogeneous at lower pH values (6−9). Siewert and Gałęzowska studied a pentacoordinate Co^{II} complex as a molecular catalyst for water oxidation in which the ligand framework contained four NH imidazole units and a pyridine group.[35] Later, Anderson's group reported a related Co^{II} complex stabilized by a tetraimidazolyl-substituted pyridine framework (**b**, Scheme 1) as a catalyst for electrochemical water oxidation from pH 7 to 9,[22] while complex **b** was found to degrade rapidly under oxidative conditions; the

Received: October 7, 2021
Revised: November 15, 2021
Published: December 2, 2021

https://doi.org/10.1021/acscatal.1c04617
ACS Catal. 2021, 11, 15068−15082

Scheme 1. Molecular Structures of Selected Cobalt(II) Molecular Precatalysts for Electrochemical Water Oxidation[a]

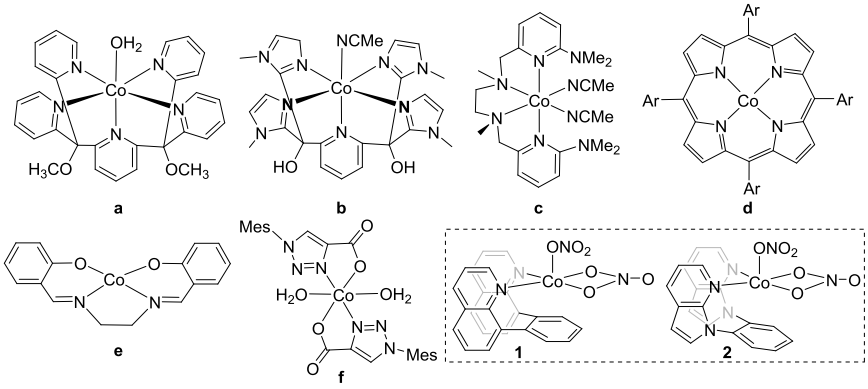

[a]**a**: refs 33 and 34; **b**: ref 22; **c**: ref 23; **d**: refs 24 and 36; **e**: ref 29; **f**: ref 37; **1** and **2**: this work.

Scheme 2. Depiction of Selected Cobalt-Heterogenized Catalysts for Electrochemical Water Oxidation[a]

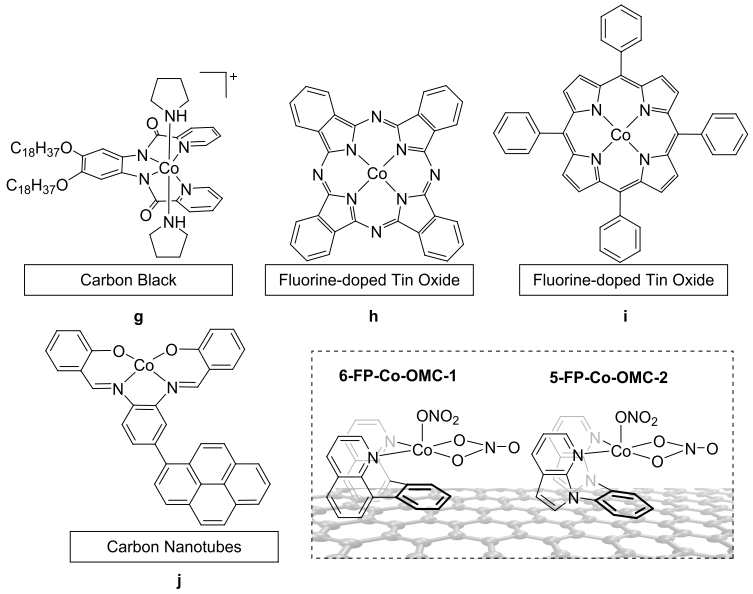

[a]**g**: ref 53; **h**: ref 56; **i**: ref 30; **j**: ref 58; **6-FP-Co-OMC-1** and **5-FP-Co-OMC-2**: this work.

authors proposed that the initial molecular complex is the active catalytic species. Recently, Yang's group reported a Co^{II} dipyridyldiamine complex (**c**, Scheme 1) with dimethylamine functional groups as pendant bases in the secondary coordination sphere as a catalyst for water oxidation in acetonitrile/water mixtures.[23] Interestingly, the analogous complex without the dimethylamine groups was found to be inactive for water oxidation, highlighting the importance of secondary sphere interactions. Another class of molecular catalysts for water oxidation is cobalt porphyrins (**d**, Scheme 1), which are active at both neutral and basic pH values.[24,36] An *N*,*N*′-bis(salicylidene)ethylenediamino Co^{II} complex was found to be an active water oxidation electrocatalyst, but in this case, the activity was attributed to the degradation of the complex under oxidative conditions at pH 11 (**e**, Scheme 1).[29] A Co^{II} complex containing two bidentate triazole carboxylate ligands was also found to be a catalyst for electrochemical water oxidation, forming an active film, in which the complex maintains its atomic structure, on the surface of the working electrode (**f**, Scheme 1).[37] Complexes based on Co^{III} precursors also have been investigated as electrochemical water oxidation precatalysts.[38−45]

Despite these advancements, the instability of molecular catalysts under oxidative conditions can pose significant challenges for their incorporation into electrolyzers.[41,46] In contrast, heterogeneous catalysts often exhibit higher electrocatalytic stability and can be directly incorporated into solid-state electrolyzers, but a major limitation of heterogeneous catalysts is the challenge associated with understanding and optimizing the structure of active sites. The integration of the molecular catalyst structure with heterogeneous materials is desirable since it offers the potential for device development presented by heterogeneous materials with the opportunity to tune catalytic active sites.[12,47,48]

Recently, research efforts have focused on the preparation of supported electrocatalysts by anchoring molecular catalysts

https://doi.org/10.1021/acscatal.1c04617
ACS Catal. 2021, 11, 15068−15082

directly to an electrode or to a carbon support using covalent and noncovalent attachment methods.[47−52] Several examples have been reported for the synthesis of cobalt-heterogenized catalysts for water oxidation via van der Waals interactions between a cobalt complex with long alkyl chains and fluorine-doped tin oxide (FTO) or carbon electrodes (see, for example, **g** in Scheme 2).[53−55] Supported Co^{II} phthalocyanine complexes are efficient molecular water oxidation electrocatalysts at pH 7 when physiosorbed onto FTO (**h**, Scheme 2)[56] or at basic pH (1 M KOH) when $\pi-\pi$-stacked onto carbon nanotubes.[57] Investigations of cobalt porphyrin complexes physiosorbed onto FTO (**i**, Scheme 2) demonstrated that the formation of a CoO_x film on the electrode is responsible for the observed catalytic water oxidation activity.[30] A pyrene-modified Co^{II} salophen complex immobilized on multiwalled carbon nanotubes (**j**, Scheme 2) was also found to degrade to cobalt hydroxides under oxidative conditions.[58] Covalent methodologies, such as direct amidation coupling, were used to immobilize Co^{III} corroles onto carbon nanotubes as efficient catalysts for electrochemical water oxidation at pH 0, 7, and 14.[59]

Immobilization of the molecular catalysts by $\pi-\pi$ stacking using various aromatic groups of ligands can boost electronic π-delocalization between molecular catalysts and carbon supports and has emerged as a strategy to increase the stability of molecular catalysts.[48] Herein, we report supported catalysts for electrochemical water oxidation by immobilizing molecular cobalt complexes on ordered mesoporous carbon (OMC) supports via $\pi-\pi$ stacking. The OMC support not only offers a substantial surface area and functional sites to immobilize cobalt complexes via π-interactions but provides an ordered tunnel matrix, which can facilitate electrochemical mass transfer.

We have recently reported studies demonstrating the ability of "capping arene" ligands to modulate the energetics of transition metal reactions that involve formal redox changes.[60−65] We have proposed that the structure of the capping arene ligand, which positions the pendant arene group and determines the extent of metal-arene bonding, can influence the relative stability of transition metal complexes in different oxidation states and geometries.[64] Given that transition metal catalysts cycle through multiple redox states during electrocatalytic water oxidation, we considered that the capping arene ligands might provide the ability to tune catalyst activity. Hence, cobalt complexes based on capping arene ligands were synthesized, characterized, and investigated as electrocatalysts for the OER. The resulting electrocatalysts were efficient for the OER, delivering a high turnover frequency (TOF) at low overpotential. Moreover, the electrocatalysts exhibited good structural stability under oxygen evolution reaction (OER) conditions, which was confirmed using X-ray absorption (XAS) spectroscopy and aberration-corrected transmission electron microscopy (TEM) characterization, although catalyst partial decomposition after hours of catalysis was observed. In addition, density function theory (DFT) calculations revealed the structural evolution of model molecular catalysts under OER conditions to delineate the catalytic process on the active sites of the electrocatalysts. Using DFT quantum mechanics calculations to probe plausible mechanisms for O−O bond formation, we determined that O−O bond formation most likely occurs through an intramolecular reductive elimination process in which oxo and hydroxo ligands on Co^{IV} couple to form a Co^{II}−OOH species. The structure of the capping arene ligand appears to influence the free energy of activation for this proposed rate-determining redox reaction.

RESULTS AND DISCUSSION

Synthesis and Characterization of "Capping Arene" Co(II) Complexes. Capping arene ligands were selected as a platform for the preparation of cobalt complexes as we considered that properties of these ligands would render them useful for applications in electrochemical water oxidation. First, capping arene ligands are likely to be stable against oxidative degradation since they lack readily oxidized aliphatic C−H bonds and other chemical groups. Second, the capping arene moiety should enable strong $\pi-\pi$ stacking, allowing the facile preparation of solid-state anodes on carbon materials. Third, the arene can potentially bind to the metal center with the dual role of providing stabilization under oxidative conditions (Scheme 3) and acting as a direct conduit of electrical

Scheme 3. Schematic of "Capping Arene" Proligands 5-FP and 6-FP Discussed in This Work

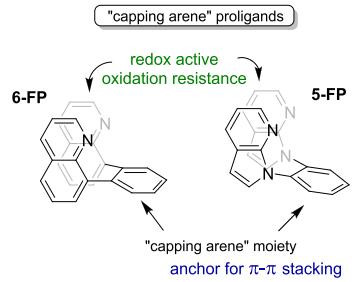

conductivity from the metal center to the carbon material. Last, the capping arene ligands provide π-active ligands similar to bipyridyls that are known shuttle redox equivalents during electrochemical processes.[66]

Two Co^{II} complexes, (6-FP)$Co(NO_3)_2$ (**1**) (6-FP = 8,8′-(1,2-phenylene)diquinoline) and (5-FP)$Co(NO_3)_2$ (**2**) (5-FP = 1,2-bis(*N*-7-azaindolyl)benzene), were synthesized by mixing the corresponding proligand 6-FP or 5-FP and $Co(NO_3)_2{\cdot}6H_2O$ in acetonitrile at room temperature. Complexes **1** and **2** were isolated as purple crystals in yields of 75% (**1**) and 45% (**2**) (Scheme 4). They have been fully characterized by paramagnetic ^1H and ^{13}C NMR spectroscopy, elemental analysis, EPR spectroscopy, SQUID magnetometry, and single-crystal X-ray diffraction. Single crystals adequate for X-ray diffraction were obtained by vapor diffusion of diethyl ether into a CH_2Cl_2 solution saturated with **1** or **2** (Figure 1). The geometry around the cobalt center in **1** can be described as distorted trigonal bipyramidal (TBP) with the value of the τ_5 distortion parameter of 0.69 significantly deviated from the ideal value of 1 for a TBP structure.[67] The equatorial plane results from the coordination of two nitrogen atoms of the 6-FP ligand and an oxygen atom from a bidentate nitrate ligand with the axial positions formed by the other oxygen from the bidentate nitrate and an oxygen atom from a monodentate nitrate ligand (Figure 1a). The Co−N bond distances, Co1−N1 2.0859(11) Å and Co1−N2 2.1224(11) Å, are comparable

https://doi.org/10.1021/acscatal.1c04617
ACS Catal. 2021, 11, 15068−15082

Scheme 4. Synthetic Routes to (6-FP)Co(NO_3)$_2$ (1, Top) (6-FP = 8,8′-(1,2-Phenylene)diquinoline) and (5-FP)Co(NO_3)$_2$ (2, Bottom) (5-FP = 1,2-Bis(*N*-7-azaindolyl)benzene)

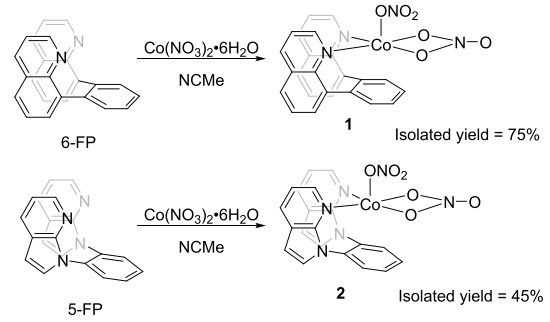

to those observed in other Co^{II} complexes with chelating pyridine-based ligands.[23] The Co−O bonds exhibit two shorter distances and one longer distance (Co1−O2 2.0420(9) Å, Co1−O4 2.0551(10) Å, and Co1−O1 2.3244(10) Å). The Co^{II} atom is located directly above C10 and C15 of the capping arene ring, but the Co−C distances of 2.921(4) Å and 2.698(5) Å are too elongated to indicate significant bonding interaction. For complex **2**, four independent molecules are found in the unit cell of the solid-state structure, displaying two different geometries around the cobalt center. Two of the molecules present distorted square-pyramidal geometries and the other two present distorted octahedral geometries, depending on whether the second nitrate is bound k^1 or k^2 to the metal center (Figure 1 and the Supporting Information). The Co−N distances range from 2.056(6) Å to 2.124(6) Å, similar to those observed for complex **1**. Analogous to complex **1**, little to no arene−Co interaction is present in complex **2**.

Complexes **1** and **2** exhibit well-behaved paramagnetic ^{1}H and ^{13}C NMR spectra. Hence, the wide-scan ^{1}H and ^{13}C NMR spectra of complexes **1** and **2** in $CDCl_3$ at room temperature display broad paramagnetically shifted peaks that are consistent with symmetric complexes. For complex **1**, peaks range from 95 to −40 ppm in the ^{1}H NMR spectrum (Figure 2a) and from 640 to 80 ppm in the ^{13}C NMR spectrum (Figure 2b,c). For complex **2**, peaks range from 140 to 0 ppm in the ^{1}H NMR spectrum and from 425 to 120 ppm in the ^{13}C NMR spectrum (Figures S1 and S2, Supporting Information). The magnetic moments (μ_{eff}) of **1** and **2** were determined by the Evans NMR method to be 3.4(2) and 4.3(2), respectively, indicating high-spin character. Magnetic susceptibility traces of **1** and **2** measured as neat polycrystalline powders are shown in Figure 3. For **1** and **2**, χT values of 2.55 and 2.52 cm^3 mol^{-1} K (μ_{eff} = 4.6μ_B and μ_{eff} = 4.5μ_B) were obtained at room temperature, respectively. These χT values are in good agreement with a high-spin (S = 3/2) Co^{II} and correspond to $g \approx 2.3$ using $\chi T \approx \frac{1}{8} g^2 S(S+1)$. The observed deviation of g from 2 is characteristic for Co^{II} and originates from spin−orbit coupling. Down to 100 K, χT values remained constant. Upon decreasing temperature, these values were reduced to 1.25 cm^3 mol^{-1} K (**1**) and 1.4 cm^3 mol^{-1} K (**2**) at 2 K, indicating large magnetic anisotropy in the samples. The insets in Figure 3 show reduced magnetization curves for **1** and **2** at constant magnetic fields of 1, 4, and 7 T, respectively. These curves superimpose at low temperatures, suggesting zero field splitting (zfs) much larger than the Zeeman splitting induced by the external magnetic fields. Both paramagnetic NMR and SQUID magnetometry are well in accordance with a Co^{II} S = 3/2 state with large zfs; this assignment is further supported by the low-temperature EPR spectra depicted in Figure S3, Supporting Information. However, μ_{eff} values obtained from solution paramagnetic NMR and polycrystalline SQUID measurements were found to be different. Moreover, frozen solution EPR and SQUID traces could not be simulated with one set of spin coupling parameters. These discrepancies indicate that complexes **1** and **2** in solution exhibit different magnetic properties and most likely also different geometric structures than in the crystalline phases.

The cyclic voltammetry of **1** (0.5 mM) was measured in MeCN under a dinitrogen atmosphere in the presence of tetrabutylammonium hexafluorophosphate as the supporting electrolyte using ferrocene as an internal standard. Complex **1** displays an irreversible oxidation peak at E_p^a = 1.09 V vs Fc^+/Fc (Figure 4a), and complex **2** displays an irreversible oxidation peak at E_p^a = 1.11 V vs Fc^+/Fc (Figure 4b), indicating that the products of oxidation are likely unstable

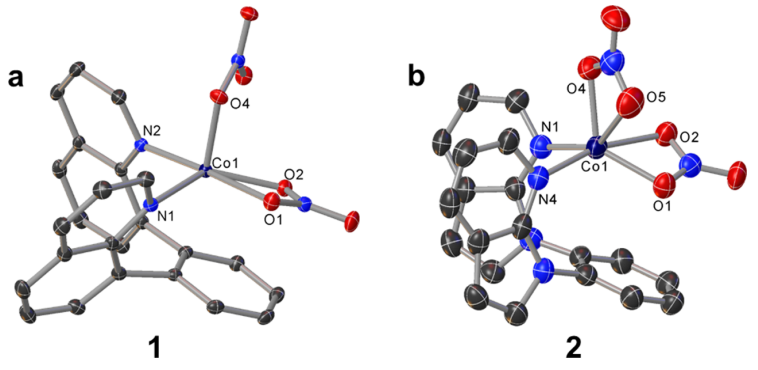

Figure 1. Single-crystal characterization of Co complexes. (a) ORTEP of (6-FP)Co(NO_3)$_2$ (**1**) with anisotropic displacement parameters set at 50% probability. Hydrogen atoms have been omitted for clarity. Selected bond lengths (Å) and angles (°) for (6-FP)Co(NO_3)$_2$ (**1**): Co1−N2 2.1224(11), Co1−N1 2.0859(11), N2−Co1−O2 124.41(4), O2−Co1−N1 135.00(4), O1−Co1−N2 176.14(4), O4−Co1−O1 81.71(4), and O4−Co1−N2 99.21(4); (b) ORTEP of (5-FP)Co(NO_3)$_2$ (**2**) with anisotropic displacement parameters set at 50% probability. Hydrogen atoms have been omitted for clarity. Selected bond lengths (Å) and angles (°) for (5-FP)Co(NO_3)$_2$ (**2**), one of the independent molecules in the unit cell of **2**: Co1−N4 2.124(6), Co1−N1 2.088(6), and N1−Co1−O1 135.7(2).

https://doi.org/10.1021/acscatal.1c04617
ACS Catal. 2021, 11, 15068−15082

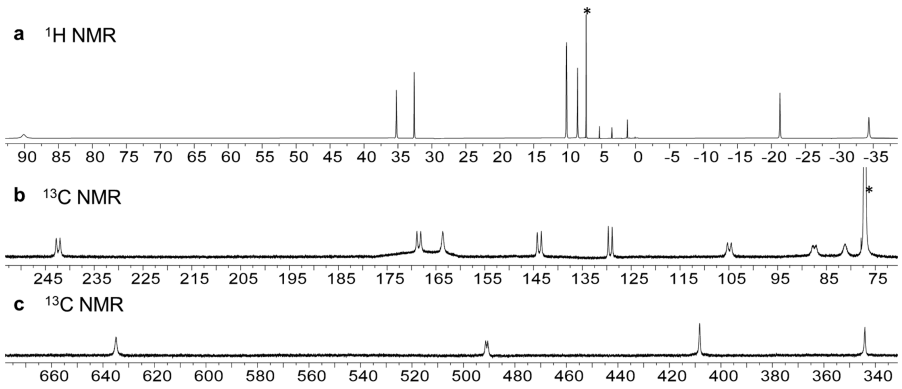

Figure 2. NMR characterization of (6-FP)Co$(NO_3)_2$. (a) ^{1}H NMR spectrum of (6-FP)Co$(NO_3)_2$ (**1**) in $CDCl_3$. (b) ^{13}C NMR spectrum from 70 to 250 ppm of (6-FP)Co$(NO_3)_2$ (**1**) in $CDCl_3$. (c) ^{13}C NMR spectrum from 330 to 680 ppm of (6-FP)Co$(NO_3)_2$ (**1**) in $CDCl_3$. The asterisk (*) indicates $CDCl_3$ in the spectra.

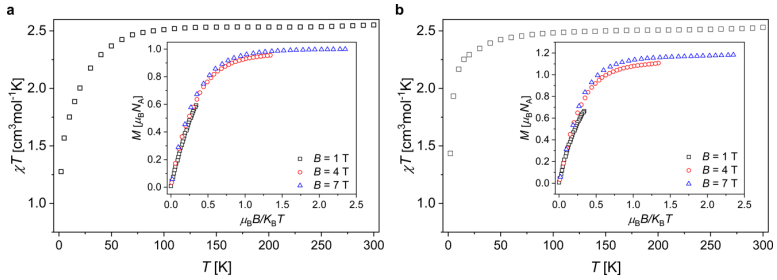

Figure 3. Magnetic susceptibility of (a) **1** and (b) **2** as χT product vs temperature. (Inset) Reduced magnetization at magnetic fields of 1 T (open square), 4 T (open circle), and 7 T (open up-pointing triangle) for **1** and **2**, respectively.

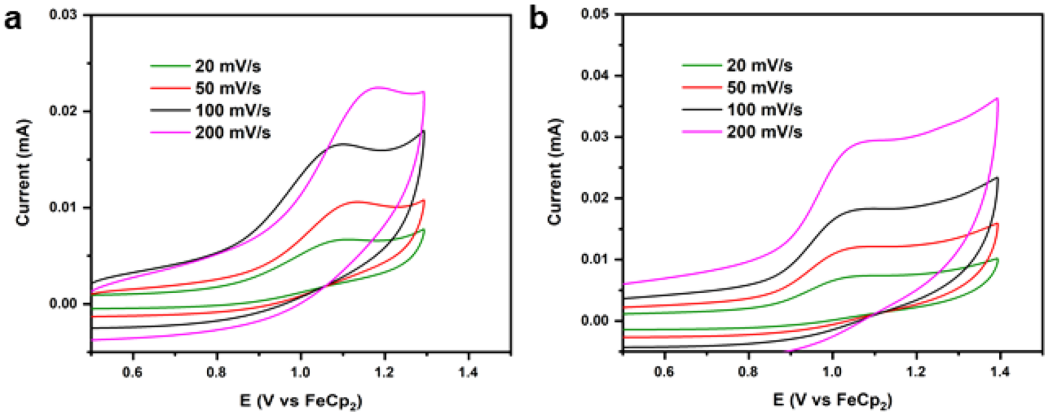

Figure 4. Electrochemical characterization of Co complexes in a homogeneous system. (a) Cyclic voltammogram of (6-FP)Co$(NO_3)_2$ (**1**) in MeCN at variable scan rates. (b) Cyclic voltammogram of (5-FP)Co$(NO_3)_2$ (**2**) in MeCN at variable scan rates.

under the electrochemical conditions. Both oxidation peaks for **1** and **2** are diffusion-controlled. Addition of 1 M KOH aqueous solution to both complexes **1** and **2** in MeCN produces a brown insoluble precipitate (most likely cobalt hydroxide), which prevented the study of molecular water oxidation.

Immobilization of "Capping Arene" Co(II) Complexes on OMC. Conductive OMC possesses a large surface area with an ordered framework structure, providing opportunities for application in heterogeneous electrocatalysis with potential advantages for mass transfer.[68] Our strategy for immobilization of Co complexes **1** and **2** involved attaching **1** or **2** on OMC via $\pi-\pi$ stacking interactions between the arene ligand platform and the carbon support. The resulting material provides a heterogenized molecular electrocatalyst for the OER. The OMC support was obtained by the carbonization of oleic acid ligand in a self-assembled Fe_3O_4 colloidal nanoparticle superlattice followed by the removal of the Fe_3O_4 template.[68] Monodisperse Fe_3O_4 nanoparticles were synthesized with oleic acid as a surface capping ligand. The TEM image in Figure S4, Supporting Information, shows that the resulting Fe_3O_4 nanoparticles have a size of 9.5 ± 0.5 nm. The

https://doi.org/10.1021/acscatal.1c04617
ACS Catal. 2021, 11, 15068−15082

three-dimensional Fe_3O_4 nanoparticle face-center cubic (fcc) superlattices were produced through slow evaporation of hexane solvent under ambient conditions,[68] which were then annealed at 500 °C in nitrogen gas to carbonize the oleic acid surfactant and subsequently washed in hydrochloric acid at 120 °C to remove the Fe_3O_4 template (Figure S5, Supporting Information). The resulting OMC material, after a further treatment at 900 °C in forming gas (5% H_2 in N_2) to enhance the electrical conductivity and degree of graphitization as we reported before,[51] shows an ordered structure with a pore size of ∼7.5 nm and a wall thickness of ∼2.5 nm (Figure 5a).

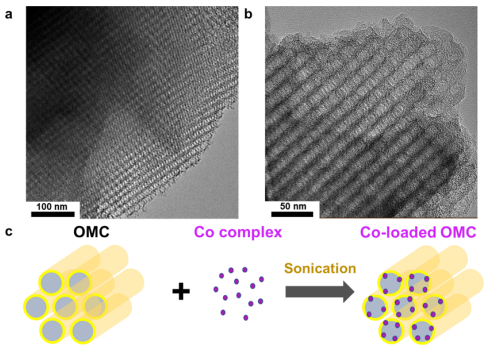

Figure 5. Morphology characterizations of OMC and Co complex-loaded OMC. (a) TEM of the OMC after 900 °C treatment in forming gas (5% H_2 in N_2). (b) TEM image of **6-FP-Co-OMC-1**. (c) Schematic illustration of immobilization of the Co complex on OMC.

The Co complex-loaded OMC was generated by sonicating the mixture of the molecular complex, OMC, and isopropanol (Figure 5b,c and Figure S6, Supporting Information). We anticipated that the Co complex attachment onto the OMC would be enhanced by $\pi-\pi$ stacking interaction, similar to our previous work on Ir complex-loaded OMC.[51] Because of the porous structure and large surface area with facilitated diffusion from sonication, the OMC material should enable a high loading of the molecular Co complexes. The resulting Co complex-loaded OMC is labeled as **6-FP-Co-OMC-1** for **1** and **5-FP-Co-OMC-2** for **2**. A control material was synthesized without FP ligand by loading $Co(NO_3)_2{\cdot}6H_2O$ onto OMC, which is marked as **$Co(NO_3)_2$-OMC-3**. As shown in Figure 5b and Figure S6, Supporting Information, TEM images of **6-FP-Co-OMC-1** and **5-FP-Co-OMC-2** exhibit well-maintained OMC structures with homogeneous dispersion of cobalt complexes in the framework. The quantitative loading of Co in these samples was carried out with ICP-OES, which is 17.1, 19, and 4.3% for **6-FP-Co-OMC-1**, **5-FP-Co-OMC-2**, and **$Co(NO_3)_2$-OMC-3**, respectively. Elemental mapping of cobalt on OMC shows homogeneous dispersion of Co on the OMC surfaces (Figures S7 and S8).

Electrocatalysis over Co Complex-Loaded OMC. The **6-FP-Co-OMC-1** and **5-FP-Co-OMC-2** catalysts were studied for the OER using a three-electrode system with a rotating disk electrode (RDE) as a working electrode. The electrochemical analyses were conducted in O_2-saturated 1 M KOH aqueous electrolyte. The linear sweep voltammetry (LSV) plot from 0.6 to 1.67 V vs reversible hydrogen electrode (RHE) at a scan rate of 10 mV s^{-1} (Figure 6a) shows that **6-FP-Co-OMC-1** and **5-FP-Co-OMC-2** deliver a substantially higher current density than **$Co(NO_3)_2$-OMC-3** and pristine OMC at the same overpotential. As shown in Figure 6a, **6-FP-Co-OMC-1** and **5-FP-Co-OMC-2** reach current densities of 34.6 and 32.0 mA cm^{-2} at an overpotential of 400 mV, which are higher than those of **$Co(NO_3)_2$-OMC-3** (1.1 mA cm^{-2}) and pristine OMC (3.5 mA cm^{-2}). The overpotential of **6-FP-Co-OMC-1** at 10 mA cm^{-2} current density was 355 mV, lower than that of **5-FP-Co-OMC-2** (370 mV). Continuous LSV scan of **6-FP-Co-OMC-1** is provided in Figure S9, indicating that the performance of the immobilized Co molecular catalyst is stabilized after 10 scans. We found that **6-FP-Co-OMC-1** and **5-FP-Co-OMC-2** exhibited similar Tafel slopes of 67 and 55 mV dec^{-1}, suggesting similar OER kinetics (Figure 6b). The Faradic efficiencies of **6-FP-Co-OMC-1** and **5-FP-Co-OMC-2** are >90% at different current densities, indicating the high energy efficiency of both catalysts (Figure 6c).

The OER TOFs over **6-FP-Co-OMC-1** and **5-FP-Co-OMC-2** are summarized in Figure 6d. **6-FP-Co-OMC-1** delivers a TOF of 0.53 s^{-1} at an overpotential of 400 mV, which is higher than **5-FP-Co-OMC-2** with a TOF of 0.32 s^{-1} at the same overpotential (Figure 6d). Both are superior to **$Co(NO_3)_2$-OMC-3**, which exhibits a TOF of 0.04 s^{-1} at 400 mV overpotential. The intrinsic activities of **6-FP-Co-OMC-1** and **5-FP-Co-OMC-2** appear to be better than many other supported Co catalysts in previous reports once overpotential is taken into account (Table 1). Also, our studies show a pronounced benefit of the capping arene ligands, as demonstrated by comparative electrocatalytic OER using **6-FP-Co-OMC-1**, **5-FP-Co-OMC-2**, and **$Co(NO_3)_2$-OMC-3**, which presented activity that is ∼10 times that of **$Co(NO_3)_2$-OMC-3**. While **6-FP-Co-OMC-1** and **5-FP-Co-OMC-2** give similar performance, the ratio of TOF using **6-FP-Co-OMC-1** versus **5-FP-Co-OMC-2** at 300, 350, and 400 mV are 3.75, 2.46, and 1.65, respectively. Assuming that the core molecular structure remains intact upon anchoring to the OMC material, these data indicate a more active site for 6-FP-Co versus 5-FP-Co, which is consistent with computational modeling of electrocatalytic water oxidation (see below).

The stability of **6-FP-Co-OMC-1** was studied with a chronoamperometry (CA) test at 300 mV overpotential. As shown in Figure 7a, the current density of the **6-FP-Co-OMC-1** catalyst retains 55% of the initial activity after 11 h of electrocatalysis. We found from TEM images in Figure 7b that the structure of OMC was maintained well with no visible nanoparticles of cobalt oxide. The high-angle annular dark field scanning TEM (HAADF-STEM) image acquired by an aberration-corrected STEM in Figure 7c shows that the catalyst after 11 h of electrocatalysis is present as a mixture of single-atom Co and cobalt oxide clusters on the OMC surface and the latter could arise from confined cobalt atomic species. Further investigation of the structure of the cobalt sites before and after the stability test was conducted by employing a spectroscopic probe of XAS. The Fourier-transformed Co K-edge extended X-ray absorption fine structure (EXAFS) of complex **1** and **6-FP-Co-OMC-1** before and after the CA stability test is presented in Figure 7d, Figures S10−S12, and Table S1, Supporting Information. The spectra of **1** and **6-FP-Co-OMC-1** exhibit very similar profiles with a predominant peak at an atomic distance of 1.59 Å corresponding to a Co−O/N bond, which is distinct to representative Co−O scattering pathways for Co oxide materials (2.4−2.5 Å).[7] The **6-FP-Co-OMC-1** material after the chronoamperometry test over 11 h exhibits similar characteristics of a Co−O/N bond with a peak at 1.62 Å while also showing new scattering

https://doi.org/10.1021/acscatal.1c04617
ACS Catal. 2021, 11, 15068−15082

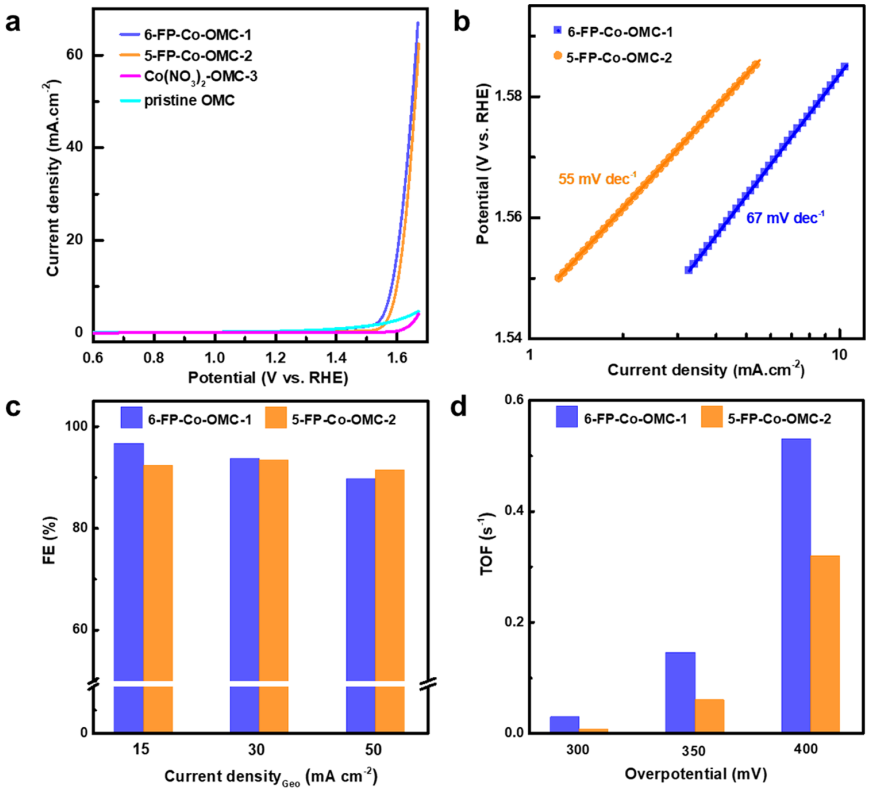

Figure 6. OER catalytic performance of Co complex-loaded OMC. (a) LSV plot of **6-FP-Co-OMC-1** (dark blue), **5-FP-Co-OMC-2** (orange), **Co(NO$_3$)$_2$-OMC-3** (pink), and pristine OMC (light blue). (b) Tafel plot of **6-FP-Co-OMC-1** (blue) and **5-FP-Co-OMC-2** (orange). (c) Faradic efficiency of **6-FP-Co-OMC-1** and **5-FP-Co-OMC-2** at different current densities. (d) TOFs of **6-FP-Co-OMC-1** and **5-FP-Co-OMC-2** at different OER overpotentials.

Table 1. TOFs of Electrocatalytic Water Oxidation Using 6-FP-Co-OMC-1 and 5-FP-Co-OMC-2 in Comparison to Reported Examples of Hybrid Co Catalysts[a]

entry	catalyst	electrolyte, pH	η (mV)	TOF (s^{-1})	reference
1	CoHβFCXCO$_2$H@Nafion film	0.1 M phosphate, 7	790	0.81(a)	25
2	CoTPP@FTO	0.1 M borate, 9.2	500	3(b)	30
3	cobalt-modified FTO	0.1 M phosphate, 7.2	800	4(c)	32
4	[Co(LOC1$_8$)(pyrr)$_2$]ClO$_4$@carbon black	1 M KOH, 14	490	1.1(d)	53
5	CoFPc@carbon cloth	0.5 M NaHCO$_3$, 7.2	770	0.45(e)	55
6	CoFPc@FTO	0.1 M phosphate, 7	770	3.6(e)	56
7	CoPc-SO$_3$H@carbon nanotubes	1 M KOH, 14	400	11.37(f)	57
8	pyrene-modified cobalt salophen@carbon nanotubes	0.1 M phosphate, 7.0	534	0.36(e)	58
9	CoO	1 M KOH, 14	370	0.04	69
10	Co$_3$O$_4$ NPs	1 M KOH, 14	507	0.08(g)	70
11	6-FP-Co-OMC-1	1 M KOH, 14	300/350/400	0.03/0.15/0.53(f)	this work
12	5-FP-Co-OMC-2	1 M KOH, 14	300/350/400	0.008/0.061/0.32(f)	this work
13	Co(NO$_3$)$_2$-OMC-3	1 M KOH, 14	300/350/400	0.004/0.009/0.042(f)	this work

[a]HβFCXCO$_2$H = 2,3,7,8,12,13,17,18-octafluoro-10-(4-(5-methoxycarbonyl-2,7-di-*tert*-butyl-9,9-dimethylxanthene))-5,15-bis(pentafluorophenyl)-corrole; CoTPP = 5,10,15,20-tetraphenyl-21*H*,23*H*-porphine cobalt(II); LOC1$_8$ = *N*,*N*′-[4,5-bis(octadecyloxy)-1,2-phenylene]dipicolineamide; pyrr = pyrrolidine; CoFPc = perfluorinated cobalt phthalocyanine; CoPc-SO$_3$H = sulfonated cobalt phthalocyanine. (a) TOF determined from the current density of CV. (b) TOF determined from CV and Co loading was determined from integration of the Co(II)/Co(III) redox wave. (c) TOF determined from controlled potential electrolysis and Co loading determined from integration of the CV wave. (d) TOF determined from O$_2$ measurements. (e) TOF determined from O$_2$ measurements and Co loading from ICP measurements. (f) TOF determined from the catalytic current from LSV and loading from ICP measurements. (g) TOF calculated from an average current density obtained from current−voltage curves.

due to cobalt oxide clusters at 2.76 Å, which indicates that the immobilized Co complex was confined on the surface of the OMC and partially evolved to Co oxide clusters under oxidative potentials. Similar phenomena were observed for complex **2** and **5-FP-Co-OMC-2** (Figures S13−S18, Supporting Information).

https://doi.org/10.1021/acscatal.1c04617
ACS Catal. 2021, 11, 15068−15082

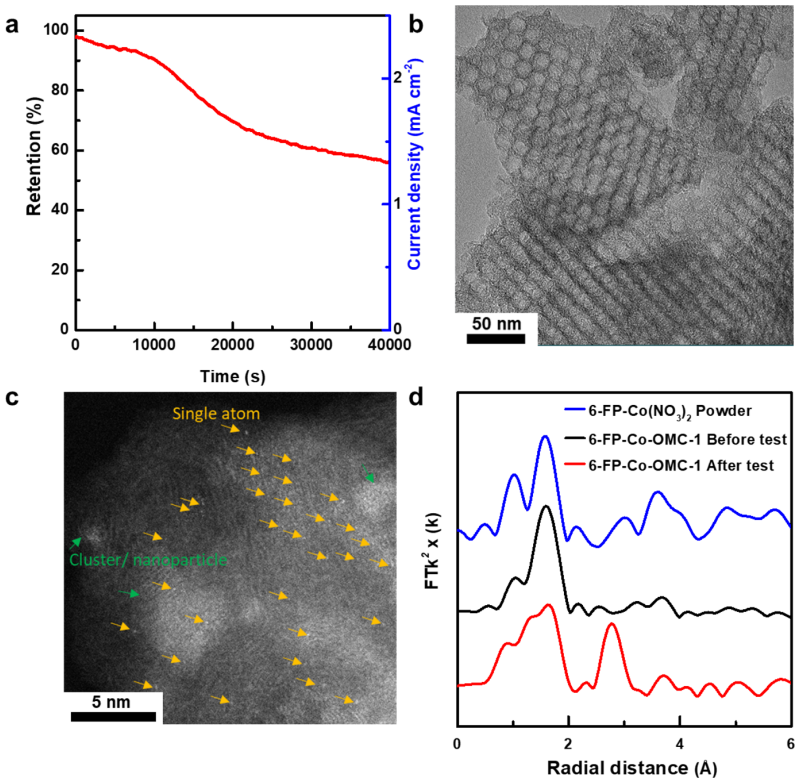

Figure 7. OER stability investigation on (6-FP)Co$(NO_3)_2$-loaded OMC. (a) Stability test of **6-FP-Co-OMC-1** with chronoamperometry (CA) test for 11 h. (b) TEM image of **6-FP-Co-OMC-1** after the CA test at 300 mV overpotential. (c) HAADF-STEM image of **6-FP-Co-OMC-1** after the CA test at 300 mV overpotential. (d) EXAFS analysis for (6-FP)Co$(NO_3)_2$ (**1**) and **6-FP-Co-OMC-1** before and after the OER test.

DFT Calculations. We utilized DFT quantum mechanics calculations to probe plausible pathways for electrocatalytic water oxidation by complexes **1** and **2**. This methodology has been previously validated to determine mechanisms and kinetics for numerous electrocatalytic processes including trinuclear Cu,[16] Co-doped TiO_2,[7] IrO_2,[71] and Fe-doped NiOOH.[72] Our computational studies aimed to determine the reaction pathway for electrocatalytic water oxidation that provides the most facile mechanism for O−O bond formation. Due to the size of the OMC-supported structure, we modeled the mechanism of electrocatalytic water oxidation using the molecular Co^{II} complexes **1** and **2**.

We modeled the mechanism of electrocatalytic water oxidation starting with the Co^{II} aqua complex (6-FP)Co$(OH)_2(H_2O)$ (Scheme 5). For (6-FP)Co$(OH)_2(H_2O)$, DFT predicts Co−N distances of 2.00 and 1.99 Å, which are similar to the experimental Co−N bond distances of 2.0859(11) Å and Co1−N2 2.1224(11) Å for **1**. For the OH ligands, DFT predicts a Co−O distance of 1.90 Å. The water ligand is positioned to form two hydrogen bonds, one with each OH ligand. Single-electron oxidation to Co^{III} and deprotonation of the H_2O ligand form (6-FP)Co$(OH)_3$ at an applied potential of 0.7 V versus RHE; the proton-coupled single-electron oxidation to Co^{III} exhibits uphill 13.0 kcal mol^{-1} free energy. The calculated complex (6-FP)Co$(OH)_3$ has three equal Co−O bond distances of 1.85 Å, and the Co−N distances are calculated to be 2.03 and 2.10 Å. A second proton-coupled single-electron oxidation to form Co^{IV} occurs through deprotonation of the axial OH group to form the oxo complex (6-FP)Co$(OH)_2(O)$. Formation of the Co^{IV} oxo complex is endergonic at 28.1 kcal mol^{-1} relative to the Co^{II} starting state and 15.1 kcal mol^{-1} relative to (6-FP)Co$(OH)_3$. Similar calculations beginning with (5-FP)Co$(OH)_2(H_2O)$ reveal only modest differences in calculated energetics (Scheme 5).

Scheme 5. DFT Free Energies at 298 K for the Oxidation of (6-FP)Co$(OH)_2(H_2O)$ (Left) and (5-FP)Co$(OH)_2(H_2O)$ (Right)[a]

[a]Free energies are calculated at 0.7 V vs RHE.

Inspection of the Co^{IV}=O species reveals the structures of the 6-FP and 5-FP complexes to be quite similar. The DFT-optimized structures are shown in Figure 8. For (6-FP)Co$(OH)_2(O)$, DFT predicts a Co=O distance of 1.73 Å; the distances between Co and the nearest C atoms of the capping arene (Co−C_{cap}) are 3.00 and 2.69 Å. For (5-FP)Co$(OH)_2(O)$, the Co=O distance is 1.72 Å and the Co-C_{cap} distances are 2.97 and 3.07 Å. As expected, the arene of the 6-FP ligand resides closer to the metal center than the arene of the 5-FP ligand. However, it appears that the capping arene does not affect the length of the Co=O bond (1.73 Å for 6-FP

https://doi.org/10.1021/acscatal.1c04617
ACS Catal. 2021, 11, 15068−15082

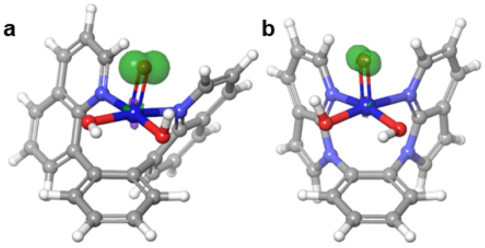

Figure 8. DFT-optimized structures of Co molecular complexes. (a) (6-FP)Co(OH)$_2$(O). (b) (5-FP)Co(OH)$_2$(O). Spin density surfaces are also provided. The spin density surface areas for (6-FP)Co(OH)$_2$(O) and (6-FP)Co(OH)$_2$(O) are 8.58 and 5.68 Å^2, respectively. Note that the oxygen spin is in a p orbital overlapping the OH at a 90° O−Co−OH dihedral angle.

and 1.72 Å for 5-FP). It is interesting to note that 6-FP must undergo significant distortion to accommodate the shorter Co−C$_{cap}$ distances, while the 5-FP ligand remains essentially symmetric about the mirror plane.

In Figure 8, we also present the spin density surfaces. As expected, the unpaired spin resides on the oxo in both structures. For the 6-FP case, the Mulliken spin population on the oxo is 1.021, while for the 5-FP complex, the Mulliken spin population on the oxo ligand is 1.024.[73] The formation of (6-FP)Co(OH)$_2$(O) prepares the complex for the calculated rate-limiting O−O bond formation step. In heterogeneous electrocatalytic water oxidation, O−O formation typically occurs through an absorbed evolution mechanism.[7] In the present molecular/homogeneous case, we studied four likely mechanisms for O−O bond formation:

1. The Co^{IV} oxo complex could undergo an intramolecular reductive O−O coupling in which the oxo and a bound hydroxo group form an O−O bond to generate a Co^{II}−OOH intermediate.
2. A two-step path could occur with the first step involving water from the first solvent shell protonating a hydroxo ligand to form (6-FP)Co(OH)(H$_2$O)(O) and a free OH$^-$. In the second step, the free hydroxide initiates nucleophilic attack on the oxo ligand to form Co^{II}-OOH.
3. A concerted path would involve O−O bond formation between external water and the oxo ligand with protonation of a hydroxo ligand occurring simultaneously. This cyclic transition state involves a proton shuttle in which mediating water accepts a proton from water, forming OOH, while simultaneously donating a proton to the hydroxo ligand to form a water molecule. This path also forms a Co^{II}−OOH product.
4. A single-step one-electron reduction in which an OH anion (already present in solution at pH 14) attacks the Co−oxo to generate Co^{III}-OOH. This is similar to the second step in mechanism 2, the difference being the final oxidation state of Co.

The calculated energetics and mechanisms for O−O bond formation are displayed in Scheme 6. For the 6-FP ligand, each pathway starts with (6-FP)Co(OH)$_2$(O), which has 28.1 kcal mol^{-1} free energy above the starting state. Path 1 involving the intramolecular reductive O−O coupling is calculated to have a free energy barrier of 36.8 kcal mol^{-1} above the starting state (or 5.1 kcal mol^{-1} relative to the Co^{IV} oxo complex). This transition state has an imaginary frequency at −346.2 cm^{-1} with an O−O distance of 1.8 Å.

Scheme 6. DFT Free Energies at 298 K for the Possible O−O Bond Formation Mechanisms: Paths 1 (Green), 2 (Orange), 3 (Red), and 4 (Blue)[a]

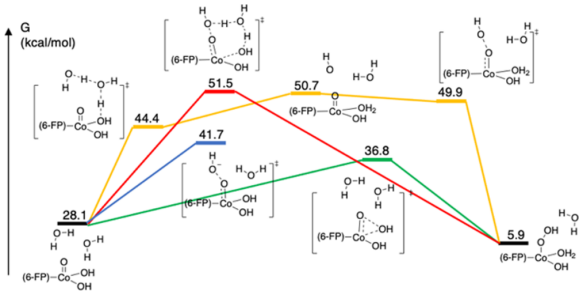

[a]Free energies are relative to the (6-FP)Co(OH)$_2$(H$_2$O) starting state. Relative energies are not to scale.

Path 2 involves two steps, the second step being rate-determining. The O−O bond formation between the free hydroxide and the Co−oxo has 49.9 kcal mol^{-1} free energy above the Co^{II} starting state (or 21.8 kcal mol^{-1} relative to the Co^{III} oxo complex). The transition state for the second step has an imaginary mode at −656.9 cm^{-1} and an O−O distance of 1.98 Å. Path 2 is clearly less favorable than path 1.

The transition state for the concerted path 3 involves an eight-membered ring in which two water molecules and the OOH ligand are formed; this free energy barrier is calculated to be 51.5 kcal mol^{-1} above the starting state (or 23.4 kcal mol^{-1} above Co^{IV}−O$^{\bullet}$). The formation of (6-FP)Co(OH)(OOH)(H$_2$O) exhibits 5.9 kcal mol^{-1} free energy above the Co^{II} starting state.

Path 4 involves a single step in which a free OH anion in solution attacks the oxo ligand to generate Co^{III}-OOH. The O−O bond formation transition state possesses 41.7 kcal mol^{-1} free energy above the Co^{II} starting state so that path 1 remains the most facile. Because our experiments are performed at pH 14, some finite concentration of OH anions is expected such that the direct nucleophilic attack of an OH anion on the Co−oxo is plausible. However, we find that the energetics are not favorable, likely because Co is reduced to Co(III) as opposed to Co(II) in path 1.

Of the four mechanisms for O−O bond formation, the intermolecular water nucleophilic attack of a hydroxy ligand outlined in path 1 provides the most facile pathway. Assuming that O−O bond formation is the rate-limiting step in catalysis, the overall free energy barrier for OER from (6-FP)Co(OH)$_2$(H$_2$O) is 36.8 kcal mol^{-1} mol at an applied potential of 0.7 V versus RHE. Interestingly, the majority of this 36.8 kcal mol^{-1} barrier is due to Co oxidation (28.1 kcal mol^{-1} contribution) as opposed to O−O bond creation (8.7 kcal mol^{-1} contribution). In a related study, DFT calculations are employed to compare the intra- and intermolecular attacks of a hydroxide onto a Co^{IV}-oxo species.[73] The intermolecular pathway was found to be lower in energy as the saturated metal center required decoordination of a pyridine before the intramolecular attack. Similar reaction pathways were also calculated for [(bpy)Cu^{II}(OH)$_2$] (bpy = 2,2′-bipyridine) where the intermolecular hydroxy attack on a Cu^{III}-oxyl was found to be favored over the intramolecular attack.[74] A more recent study on the mechanism of [(bpy)Cu^{II}(OH)$_2$] water oxidation finds the intramolecular attack to be energetically favorable and attributes the formation of the O−O bond to the

https://doi.org/10.1021/acscatal.1c04617
ACS Catal. 2021, 11, 15068−15082

coupling of the oxyl moiety with a bound hydroxide ligand in an analogous manner to our proposed mechanism.[75]

We perform the identical analysis for Co-catalyzed OER with the 5-FP ligand. Starting with (5-FP)Co(OH)$_2$(H$_2$O) at 0.0 kcal mol^{-1}, oxidation to (5-FP)Co(OH)$_3$ is endergonic at 11.1 kcal mol^{-1}; further oxidation to (5-FP)Co(OH)$_2$(O) exhibits uphill to 28.2 kcal mol^{-1} free energy (Scheme 7).

Scheme 7. DFT Free Energies at 298 K for the Possible O−O Bond Formation Mechanisms: Paths 1 (Green), 2 (Orange), 3 (Red), and 4 (Blue)[a]

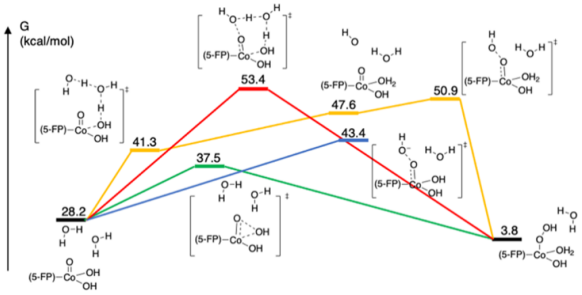

[a]Free energies are relative to the (5-FP)Co(OH)$_2$(H$_2$O) starting state. Relative energies are not to scale.

Recall that oxidation from Co^{II} to Co^{IV}=O with the 6-FP ligand has uphill 28.1 kcal mol^{-1} free energy, indicating that the capping arene identity barely affects the energetics of Co^{II} to Co^{IV} oxidation. With the oxo generated, we evaluated the four O−O bond formation pathways: (1) intramolecular reductive elimination, (2) stepwise OH protonation followed by OOH formation, (3) concerted OOH formation and OH protonation via a two-water proton shuttle, and (4) direct nucleophilic attack of the oxo by a free OH anion in solution (Scheme 7). With the 5-FP ligand, intramolecular reductive coupling requires a barrier of 37.5 kcal mol^{-1} relative to (5-FP)Co(OH)$_2$(H$_2$O). For path 2, OH protonation requires a barrier of 41.3 kcal mol^{-1}; the following OOH formation requires a barrier of 50.9 kcal mol^{-1}. Concerted OH protonation and OOH formation via the proton shuttle require a barrier of 53.4 kcal mol^{-1}. Finally, the direct attack of a free OH anion on the oxo ligand requires a free energy barrier of 43.4 kcal mol^{-1}; again, the high pH justifies the presence of OH anions in solution. The first three O−O bond-forming pathways result in the formation of (5-FP)Co(OH)(OOH)(H$_2$O), which has 3.8 kcal mol^{-1} free energy above the starting state. The barrier for intramolecular reductive coupling is the lowest of the four O−O bond formation mechanisms, just as found for the 6-FP ligand.

We note that the free energy barrier for intramolecular reductive coupling is 0.7 kcal/mol lower for the 6-FP ligand compared to the 5-FP ligand. If we ignore Co^{II} to Co^{IV} oxidation, we see that O$_2$ formation through intramolecular reductive coupling with 6-FP requires a barrier of 8.7 kcal mol^{-1}; with the 5-FP ligand, this barrier is 9.3 kcal mol^{-1} (4.2 kcal mol^{-1} higher). The 6-FP transition state has an O−O distance of 1.80 Å, while the two Co−O distances are equal at 1.95 Å (Figure 9). In the 5-FP transition state, the O−O distance is much longer at 1.96 Å. Additionally, the Co−O distances in the 5-FP transition state are substantially different; the Co−hydroxy distance is 2.28 Å, while the Co−oxo distance is 1.74 Å. The 5-FP transition state prefers an asymmetric

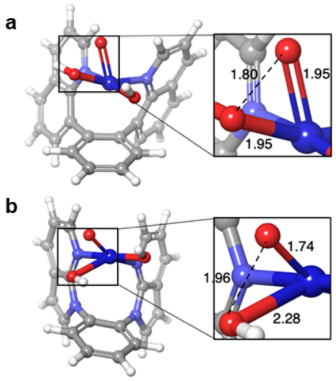

Figure 9. DFT-optimized transition states for O−O bond generation via intramolecular reductive elimination. (a) 6-FP-Co system. (b) 5-FP-Co system. These calculations were performed with implicit PBF solvation plus two explicit water molecules, which are omitted from the graphic for clarity. Lengths are in Å.

reductive coupling in which the Co−OH and Co=O distances are unique, while the 6-FP transition state appears more symmetric about the O−Co−O angle, which seems to provide a more facile route for O−O bond creation; this suggests the that the 6-FP ligand reduces the bond order between Co and the oxo significantly, allowing reductive O−O coupling to completely liberate the ligand. This is likely because the capping arene of the 6-FP ligand resides closer to the Co center and may occupy the Co−oxo antibonding orbital, consequently reducing the bonding between Co and the oxo. Conversely, the 5-FP ligand does not seem to affect the Co−oxo bond order (likely because the 5-FP cap resides further from Co and does not occupy the Co−oxo antibonding orbital) such that reductive O−O coupling reduces the bond from the second order to the first order. This correlates with the experimentally observed trend that 6-FP-ligated Co **6-FP-Co-OMC-1** produces O$_2$ more rapidly than the 5-FP-ligated Co **5-FP-Co-OMC-2**. This is consistent with the molecular motifs of (5-FP)Co and (6-FP)Co being maintained upon bonding to the OMC material.

CONCLUSIONS

The well-defined cobalt catalytic centers of (6-FP)Co(NO$_3$)$_2$ (**1**) and (5-FP)Co(NO$_3$)$_2$ (**2**) were effectively immobilized on conductive OMC, likely via $\pi-\pi$ interactions, and were found to be active catalysts for electrocatalytic OER. The resultant catalysts were investigated with ex situ XAS, demonstrating reasonable stability and slow degradation of the supported complexes under the studied conditions (1 M KOH, pH 14) to cobalt oxide clusters after 11 h of electrolysis. Theoretical DFT calculations revealed the formation of an intermediate Co^{IV} oxo species that can be converted to the hydroperoxo via intermolecular O−O reductive coupling between the oxo ligands and a hydroxide ligand. Our calculations suggest an explanation for the increased activity for **6-FP-Co-OMC-1** compared with **5-FP-Co-OMC-2**. The structure of the 6-FP ligand provides more facile O−O bond formation through increased interaction of the capping arene π space and the Co−oxo antibonding orbital. Taken together, our experimental and theoretical results demonstrate an immobilization method for the heterogenization of molecular catalysts on conductive OMC and provide a strategy for further exploration of the use

https://doi.org/10.1021/acscatal.1c04617
ACS Catal. 2021, 11, 15068−15082

of capping arene ligands that are designed to optimize electrocatalytic water oxidation.

EXPERIMENTAL SECTION

Chemicals and Materials. $FeCl_3·6H_2O$ (98%), 1-octadecene (ODE, 90%), and oleic acid (OAc, 90%) were purchased from Sigma-Aldrich. Hexane (ACS-certified), 2-propanol (IPA, ACS-certified), KOH (ACS-certified), ethanol (200 proof), and hydrochloric acid (HCl) were purchased from Fisher Scientific. Sodium oleate was obtained from Tokyo Chemical Industry.

General Methods. All reagents and solvents were purchased from commercial sources and used without further purification, unless stated otherwise. The proligands 5-FP and 6-FP were synthesized as previously described.[64,76] The UV−Vis absorption spectra were recorded using a Cary 60 UV−Vis spectrophotometer. The NMR spectra were referenced to tetramethylsilane (TMS) using residual proton signals (^{1}H NMR) or ^{13}C resonances (^{13}C NMR) of the deuterated solvents and were recorded using a Bruker AV800 spectrometer.

Synthesis of Fe_3O_4 Nanoparticles. Monodisperse Fe_3O_4 nanoparticles were synthesized according to a previously reported work.[50] Iron oleate was first prepared by reacting $FeCl_3·6H_2O$ and sodium oleate with the mixture solvent of hexane, ethanol, and DI water at 50 °C for 4 h. The Fe_3O_4 synthesis was carried out in a standard Schlenk line with moisture-free condition. The mixture of iron oleate (3.2 g), ODE (20 mL), and oleic acid (0.64 mL) was heated under vacuum to 100 °C and maintained at the temperature for 1 h to remove impurities. The system was then switched to a N_2 atmosphere, heated to 310 °C, and kept at the temperature for 1 h. Fe_3O_4 was further washed twice with IPA and separated by centrifugation. The Fe_3O_4 nanoparticles were dispersed in hexane and stored for further use.

OMC Preparation. The OMC was prepared by using a superlattice template of Fe_3O_4 nanoparticles. Hexane dispersion of Fe_3O_4 nanoparticles was placed in a ceramic boat with one glass slide covered on the top. The solvent was slowly evaporated in ambient conditions, which leads to the formation of a self-assembled superlattice. The carbonization of the oleic acid surfactant bound on nanoparticles was carried out in N_2 under 500 °C for 2 h. The obtained product was further washed with concentrated HCl at 120 °C for the removal of the Fe_3O_4 template, leading to OMC. The OMC material was subsequently treated in forming gas at 900 °C for 2 h to enhance the graphitization degree and conductivity.

Synthesis of (6-FP)$Co(NO_3)_2$ (1). 6-FP (55.2 mg, 0.166 mmol) was added to a purple solution of $Co(NO_3)_2·6H_2O$ (48.2 mg, 0.166 mmol) in acetonitrile (10 mL) and stirred overnight at room temperature, with no color change observed throughout the reaction. The solvent was removed in vacuo, and the resulting solid was extracted into dichloromethane, resulting in a violet solution (10 mL). After filtration through a fine porosity frit, crystals were obtained by the vapor diffusion method using diethyl ether. After 2 days at room temperature, bright purple crystals suitable for X-ray diffraction studies were obtained (64 mg, 75%). ^{1}H NMR (800 MHz, $CDCl_3$; all peaks appear as broad singlets) δ 90.2, 35.2, 32.6, 10.2, 10.1, 8.5, −21.3, −34.3. ^{13}C NMR (201 MHz, $CDCl_3$) δ 635.0 (br s), 491.0 (d, J = 168 Hz), 408.3 (br s), 344.1 (br s), 242.6 (d, J = 157 Hz), 168.7 (d, J = 157 Hz), 163.8 (br s), 144.0 (d, J = 167 Hz), 129.5 (d, J = 162 Hz), 105.1 (d, J = 153 Hz), 87.6 (d, J = 137 Hz), 81.4 (br s). μ_{eff} (Evans, $CDCl_3$, 25 °C) = 3.4(2) μB. Elemental analysis $C_{24}H_{26}CoN_4O_6$ (515.347): calcd.: C, 55.94; H, 3.13; N, 10.87; found: C, 55.95; H, 3.19; N, 10.49.

Synthesis of (5-FP)$Co(NO_3)_2$ (2). 5-FP (93.6 mg, 0.302 mmol) was added to a purple solution of $Co(NO_3)_2·6H_2O$ (91.7 mg, 0.315 mmol) in acetonitrile (10 mL) and stirred overnight at room temperature, with no color change observed throughout the reaction. The solvent was removed in vacuo, and the resulting solid was extracted into dichloromethane, resulting in a violet solution (10 mL). After filtration, crystals were obtained by the vapor diffusion method using diethyl ether. After 2 days at room temperature, bright purple crystals suitable for X-ray diffraction studies were obtained (66.7 mg, 45%). ^{1}H NMR (800 MHz, $CDCl_3$; all peaks appear as broad singlets) δ 135.2, 34.8, 19.4, 8.2, 5.5, 4.0, 2.0. ^{13}C NMR (201 MHz, $CDCl_3$) δ 421.4 (br d, J = 170 Hz), 373.4 (br s), 205.4 (br s), 172.7 (br s), 151.2 (d, J = 178 Hz), 148.7 (d, J = 165 Hz), 144.5 (br s), 137.7 (d, J = 164 Hz), 124.7 (br d, J = 145 Hz), 121.1 (d, J = 190 Hz). μ_{eff} (Evans, $CDCl_3$, 25 °C) = 4.3(2) μB. Elemental analysis $C_{20}H_{14}CoN_6O_6$ (493.30): calcd.: C, 48.70; H, 2.86; N, 17.04; found: C, 48.78; H, 3.01; N, 16.69.

SQUID Magnetometry. The temperature-dependent magnetization of **1** and **2** was measured as neat polycrystalline powder samples of solid material immobilized in eicosane by using a Superconducting Quantum Interference Device (SQUID, MPMS-7, Quantum Design, calibrated with a standard palladium reference sample, error < 2%) in the temperature range from 2 K to 300 K under a constant magnetic field of 1 T. The reduced magnetization data were obtained under constant magnetic fields of 1, 4, and 7 T.

EPR Spectroscopy. X-band cw EPR spectra were obtained using an X-band Bruker Elexsys E500 EPR spectrometer equipped with an ER4116DM dual mode resonator and an ESR 900 He cryostat. A total of 1.9 mg of **1** and **2** was dissolved in 1.5 mL of a 2:1 solvent mixture of toluene and $CHCl_3$ in a glove box. Two hundred microliters of each sample was transferred into standard EPR tubes for measurements. The EPR spectra were obtained at 10 K using a microwave frequency of 9.64 GHz, a microwave power of 20 mW, a lock-in modulation amplitude of 0.7 mT, a time constant of 40.96 ms, 4096 points, and a modulation frequency of 100 KHz.

Co-Loaded OMC Preparation. The mixture of Co molecular complex and OMC (weight ratio, 1/1) was dispersed in IPA and sonicated for 0.5 h. The Co-loaded OMC was collected by centrifugation and washed one more time with IPA. The precipitant was dried in ambient conditions and stored for electrocatalyst ink preparation. The loading of Co was measured with ICP-OES analysis.

Electrocatalytic OER Measurement. All electrocatalytic performance was studied at room temperature in the O_2-saturated 1.0 M KOH electrolyte. The testing cell is a three-electrode setup, including a glassy carbon working electrode, a Pt foil counter electrode, and a Hg/HgO (1.0 M KOH) reference electrode. The electrochemical characterization was conducted with a BioLogic (Model VMP3) potential station. The electrocatalyst ink was prepared by sonicating Co-loaded OMC (concentration of 5 mg ml^{-1}), IPA, and Nafion solution. The volume ratio of Nafion/IPA is 1/100. The glassy carbon electrode was polished with aluminum slurry before working electrode preparation. Electrocatalyst ink of 20 μL was spin-cast on glassy carbon. All the potentials were reported vs reversible hydrogen electrode (RHE) using the equation E(vs

https://doi.org/10.1021/acscatal.1c04617
ACS Catal. 2021, 11, 15068−15082

RHE) = E(vs HgO) + 0.926 V, where 0.926 V is the potential difference between the Hg/HgO (1.0 M KOH) reference electrode and RHE in 1.0 M KOH. The overpotential (η) for OER at a specific current density was calculated using the equation $\eta = E(\text{vs RHE}) - 1.23$ V. The OER activity was evaluated by the linear sweep voltammetry (LSV) test from 0.6 to 1.7 V vs RHE at a scan rate of 10 mV s^{-1}. The stability of catalysts was studied by the chronoamperometry test at a constant potential of 1.53 V vs RHE for 11 h. TOF was estimated according to the equation $\text{TOF} = \frac{j_{\text{Geo}} \times s}{4 \times N_{\text{Co-atom}} \times F}$, where j_{Geo} is the geometric current density on the LSV plot, s is the geometric area of the working electrode, $N_{\text{Co-atom}}$ is the amount of Co atoms obtained from the loading amount according to the ICP characterization result, and F is Faraday's constant.

Material Characterization. TEM images were characterized on an FEI Spirit (120 kV). HAADF-STEM images were obtained on a Hitachi HD2700C with a probe Cs corrector (200 kV) in the Center for Functional Nanomaterials at Brookhaven National Lab. Mass loading amounts of Co complexes on OMC were taken with inductively coupled plasma optical emission spectrometry (ICP-OES) on a PerkinElmer Avio-200 ICP spectrometer. Elemental mapping of Co was characterized with an FEI Quanta 650 at 5 keV. The ex situ Co K-edge EXAFS spectra were collected from a synchrotron X-ray source in the fluorescence mode at the beamline 20BM of Advanced Photon Source at the Argonne National Laboratory. The post-processing of EXAFS raw data was carried out with the ATHENA program based on a standard procedure.[77] The least-squares curve fitting analysis of the EXAFS $\chi(k)$ data was performed by the ARTEMIS program. The fitting model was built based on structural information from single-crystal X-ray diffraction.

Computational Methods. All density functional theory calculations were performed using Jaguar v10.9 software[78] by Schrodinger Inc. Geometry optimizations were performed using the B3LYP hybrid functional[79] with the Grimme–Becke–Johnson D3 correction[80] for London dispersion. Co was modeled with the Los Alamos small-core pseudopotential[81,82] of triple-zeta quality augmented with diffuse functions; all other atoms were described by the 6-311G** basis set.[79] Following geometry optimizations, single-point energies (SPEs) were calculated with the M06-2X functional[83] (again with the D3 correction). Co was again described by the small-core triple-zeta pseudopotential, this time augmented with polarization and diffuse functions. All other atoms were described by the 6-311G**++ basis set (designated LACV3P**++ in Jaguar). SPEs included solvent effects described by the Poisson–Boltzmann factor (PBF) implicit solvent model;[84] solvent parameters matching water were used. SPEs were accompanied by frequency calculations, which served to confirm intermediate and transition states, as well as predict thermochemical properties at 298 K.

■ ASSOCIATED CONTENT

Supporting Information

The Supporting Information is available free of charge at https://pubs.acs.org/doi/10.1021/acscatal.1c04617.

Additional data and details of single-crystal X-ray diffraction experiments, computational studies, and figures displaying the spectra and results of microscopy and electrochemistry (PDF)

Crystallographic data for **1** and **2** (CIF)

■ AUTHOR INFORMATION

Corresponding Authors

William A. Goddard III − *Materials and Process Simulation Center, Department of Chemistry, California Institute of Technology, Pasadena, California 91125, United States;* orcid.org/0000-0003-0097-5716; Email: wag@caltech.edu

Sen Zhang − *Department of Chemistry, University of Virginia, Charlottesville, Virginia 22904, United States;* orcid.org/0000-0002-1716-3741; Email: sz3t@virginia.edu

T. Brent Gunnoe − *Department of Chemistry, University of Virginia, Charlottesville, Virginia 22904, United States;* orcid.org/0000-0001-5714-3887; Email: tbg7h@virginia.edu

Authors

Chang Liu − *Department of Chemistry, University of Virginia, Charlottesville, Virginia 22904, United States;* orcid.org/0000-0002-7568-0608

Ana M. Geer − *Department of Chemistry, University of Virginia, Charlottesville, Virginia 22904, United States*

Christopher Webber − *Department of Chemistry, University of Virginia, Charlottesville, Virginia 22904, United States*

Charles B. Musgrave III − *Materials and Process Simulation Center, Department of Chemistry, California Institute of Technology, Pasadena, California 91125, United States;* orcid.org/0000-0002-3432-0817

Shunyan Gu − *Department of Chemistry, University of Virginia, Charlottesville, Virginia 22904, United States;* orcid.org/0000-0002-3625-1042

Grayson Johnson − *Department of Chemistry, University of Virginia, Charlottesville, Virginia 22904, United States;* orcid.org/0000-0001-5229-1135

Diane A. Dickie − *Department of Chemistry, University of Virginia, Charlottesville, Virginia 22904, United States;* orcid.org/0000-0003-0939-3309

Sonia Chabbra − *EPR Research Group, Max Planck Institute for Chemical Energy Conversion, Mülheim an der Ruhr 45470, Germany;* orcid.org/0000-0001-6184-2779

Alexander Schnegg − *EPR Research Group, Max Planck Institute for Chemical Energy Conversion, Mülheim an der Ruhr 45470, Germany;* orcid.org/0000-0002-2362-0638

Hua Zhou − *X-ray Science Division, Advanced Photon Source, Argonne National Laboratory, Lemont, Illinois 60439, United States*

Cheng-Jun Sun − *X-ray Science Division, Advanced Photon Source, Argonne National Laboratory, Lemont, Illinois 60439, United States*

Sooyeon Hwang − *Center for Functional Nanomaterials, Brookhaven National Laboratory, Upton, New York 11973, United States;* orcid.org/0000-0001-5606-6728

Complete contact information is available at: https://pubs.acs.org/10.1021/acscatal.1c04617

Author Contributions

#C.L. and A.M.G. contributed equally to this work.

Notes

The authors declare no competing financial interest.

https://doi.org/10.1021/acscatal.1c04617
ACS Catal. 2021, 11, 15068−15082

■ ACKNOWLEDGMENTS

This work was primarily supported by the U.S. National Science Foundation (CBET-1805022). C.B.M. and W.A.G. also received support from NSF (CBET-2005250). We thank Andreas Göbels and Dr. Eckhard Bill (MPI CEC) for conducting the SQUID measurements and Nikolai Kochetov (MPI CEC) for the help with SQUID data evaluation. This research used the resources of the Advanced Photon Source, an Office of Science User Facility operated for the US Department of Energy (DOE) Office of Science by the Argonne National Laboratory, and was supported by the US DOE under contract no. DE-AC02-06CH11357. This research used resources of the Center for Functional Nanomaterials (CFN), which is a U.S. Department of Energy Office of Science User Facility, at Brookhaven National Laboratory under contract no. DE-SC0012704.

■ REFERENCES

(1) Agency, I. E. *World Energy Outlook 2020*. 2020.
(2) Spitler, M. T.; Modestino, M. A.; Deutsch, T. G.; Xiang, C. X.; Durrant, J. R.; Esposito, D. V.; Haussener, S.; Maldonado, S.; Sharp, I. D.; Parkinson, B. A.; Ginley, D. S.; Houle, F. A.; Hannappel, T.; Neale, N. R.; Nocera, D. G.; McIntyre, P. C. Practical challenges in the development of photoelectrochemical solar fuels production. *Sustainable Energy Fuels* **2020**, *4*, 985−995.
(3) Ye, S.; Ding, C.; Li, C. Chapter One - Artificial photosynthesis systems for catalytic water oxidation. In *Adv. Inorg. Chem.*, van Eldik, R.; Hubbard, C. D., Eds. Academic Press: 2019; Vol. *74*, pp. 3−59, DOI: 10.1016/bs.adioch.2019.03.007.
(4) Tsao, J. Y.; Schubert, E. F.; Fouquet, R.; Lave, M. The electrification of energy: Long-term trends and opportunities. *MRS Energy Sustainable* **2018**, *5*, No. E7.
(5) Lewis, N. S.; Nocera, D. G. Powering the planet: Chemical challenges in solar energy utilization. *Proc. Natl. Acad. Sci. U. S. A.* **2006**, *103*, 15729−15735.
(6) Chen, F.-Y.; Wu, Z.-Y.; Adler, Z.; Wang, H. Stability challenges of electrocatalytic oxygen evolution reaction: From mechanistic understanding to reactor design. *Joule* **2021**, *5*, 1704−1731.
(7) Liu, C.; Qian, J.; Ye, Y.; Zhou, H.; Sun, C.-J.; Sheehan, C.; Zhang, Z.; Wan, G.; Liu, Y.-S.; Guo, J.; Li, S.; Shin, H.; Hwang, S.; Gunnoe, T. B.; Goddard, W. A.; Zhang, S. Oxygen evolution reaction over catalytic single-site Co in a well-defined brookite TiO_2 nanorod surface. *Nat. Catal.* **2021**, *4*, 36−45.
(8) Zhang, H.; Tian, W.; Duan, X.; Sun, H.; Liu, S.; Wang, S. Catalysis of a single transition metal site for water oxidation: From mononuclear molecules to single atoms. *Adv. Mater.* **2020**, *32*, 1904037.
(9) Matheu, R.; Garrido-Barros, P.; Gil-Sepulcre, M.; Ertem, M. Z.; Sala, X.; Gimbert-Suriñach, C.; Llobet, A. The development of molecular water oxidation catalysts. *Nat. Rev. Chem.* **2019**, *3*, 331−341.
(10) Zhang, Q.; Guan, J. Mono−/Multinuclear Water Oxidation Catalysts. *ChemSusChem* **2019**, *12*, 3209−3235.
(11) Ye, S.; Ding, C.; Liu, M.; Wang, A.; Huang, Q.; Li, C. Water oxidation catalysts for artificial photosynthesis. *Adv. Mater.* **2019**, *31*, 1902069.
(12) Zahran, Z. N.; Tsubonouchi, Y.; Mohamed, E. A.; Yagi, M. Recent advances in the development of molecular catalyst-based anodes for water oxidation toward artificial photosynthesis. *ChemSusChem* **2019**, *12*, 1775−1793.
(13) Blakemore, J. D.; Crabtree, R. H.; Brudvig, G. W. Molecular catalysts for water oxidation. *Chem. Rev.* **2015**, *115*, 12974−13005.
(14) Zhang, L.-H.; Mathew, S.; Hessels, J.; Reek, J. N. H.; Yu, F. Homogeneous catalysts based on first-row transition-metals for electrochemical water oxidation. *ChemSusChem* **2021**, *14*, 234−250.
(15) Kärkäs, M. D.; Åkermark, B. Water oxidation using earth-abundant transition metal catalysts: opportunities and challenges. *Dalton Trans.* **2016**, *45*, 14421−14461.
(16) Geer, A. M.; Musgrave, C., III; Webber, C.; Nielsen, R. J.; McKeown, B. A.; Liu, C.; Schleker, P. P. M.; Jakes, P.; Jia, X.; Dickie, D. A.; Granwehr, J.; Zhang, S.; Machan, C. W.; Goddard, W. A.; Gunnoe, T. B. Electrocatalytic water oxidation by a trinuclear copper(II) complex. *ACS Catal.* **2021**, *11*, 7223−7240.
(17) Kondo, M.; Tatewaki, H.; Masaoka, S. Design of molecular water oxidation catalysts with earth-abundant metal ions. *Chem. Soc. Rev.* **2021**, *50*, 6790−6831.
(18) Gil-Sepulcre, M.; Garrido-Barros, P.; Oldengott, J.; Funes-Ardoiz, I.; Bofill, R.; Sala, X.; Benet-Buchholz, J.; Llobet, A. Consecutive ligand-based electron transfer in new molecular copper-based water oxidation catalysts. *Angew. Chem., Int. Ed.* **2021**, *60*, 18639−18644.
(19) Xie, L.; Zhang, X.-P.; Zhao, B.; Li, P.; Qi, J.; Guo, X.; Wang, B.; Lei, H.; Zhang, W.; Apfel, U.-P.; Cao, R. Enzyme-inspired iron porphyrins for improved electrocatalytic oxygen reduction and evolution reactions. *Angew. Chem., Int. Ed.* **2021**, *60*, 7576−7581.
(20) Li, X.; Zhang, X.-P.; Guo, M.; Lv, B.; Guo, K.; Jin, X.; Zhang, W.; Lee, Y.-M.; Fukuzumi, S.; Nam, W.; Cao, R. Identifying intermediates in electrocatalytic water oxidation with a manganese corrole complex. *J. Am. Chem. Soc.* **2021**, *143*, 14613−14621.
(21) Shahadat, H. M.; Younus, H. A.; Ahmad, N.; Zhang, S.; Zhuiykov, S.; Verpoort, F. Macrocyclic cyanocobalamin (vitamin B12) as a homogeneous electrocatalyst for water oxidation under neutral conditions. *Chem. Commun.* **2020**, *56*, 1968−1971.
(22) McMillion, N. D.; Wilson, A. W.; Goetz, M. K.; Chang, M.-C.; Lin, C.-C.; Feng, W.-J.; McCrory, C. C. L.; Anderson, J. S. Imidazole for pyridine substitution leads to enhanced activity under milder conditions in cobalt water oxidation electrocatalysis. *Inorg. Chem.* **2019**, *58*, 1391−1397.
(23) Khosrowabadi Kotyk, J. F.; Hanna, C. M.; Combs, R. L.; Ziller, J. W.; Yang, J. Y. Intramolecular hydrogen-bonding in a cobalt aqua complex and electrochemical water oxidation activity. *Chem. Sci.* **2018**, *9*, 2750−2755.
(24) Wang, D.; Groves, J. T. Efficient water oxidation catalyzed by homogeneous cationic cobalt porphyrins with critical roles for the buffer base. *Proc. Natl. Acad. Sci. U. S. A.* **2013**, *110*, 15579−15584.
(25) Dogutan, D. K.; McGuire, R.; Nocera, D. G. Electocatalytic water oxidation by cobalt(III) hangman β-octafluoro corroles. *J. Am. Chem. Soc.* **2011**, *133*, 9178−9180.
(26) Kanan, M. W.; Nocera, D. G. In situ formation of an oxygen-evolving catalyst in neutral water containing phosphate and Co^{2+}. *Science* **2008**, *321*, 1072−1075.
(27) Yu, M.; Budiyanto, E.; Tüysüz, H. Principles of water electrolysis and recent progress in cobalt-, nickel-, and iron-based oxides for the oxygen evolution reaction. *Angew. Chem., Int. Ed.* **2021**, *6*, 2−26.
(28) Blackman, A. G. Cobalt: inorganic & coordination chemistry. In *Encyclopedia of Inorganic Chemistry*; John Wiley & Sons, Ltd., 2006.
(29) Najafpour, M. M.; Feizi, H. Water oxidation catalyzed by two cobalt complexes: new challenges and questions. *Catal. Sci. Technol.* **2018**, *8*, 1840−1848.
(30) Daniel, Q.; Ambre, R. B.; Zhang, B.; Philippe, B.; Chen, H.; Li, F.; Fan, K.; Ahmadi, S.; Rensmo, H.; Sun, L. Re-investigation of cobalt porphyrin for electrochemical water oxidation on FTO surface: formation of CoO_x as active species. *ACS Catal.* **2017**, *7*, 1143−1149.
(31) Wang, J.-W.; Sahoo, P.; Lu, T.-B. Reinvestigation of water oxidation catalyzed by a dinuclear cobalt polypyridine complex: Identification of CoO_x as a real heterogeneous catalyst. *ACS Catal.* **2016**, *6*, 5062−5068.
(32) Kent, C. A.; Concepcion, J. J.; Dares, C. J.; Torelli, D. A.; Rieth, A. J.; Miller, A. S.; Hoertz, P. G.; Meyer, T. J. Water oxidation and oxygen monitoring by cobalt-modified fuorine-Doped tin oxide electrodes. *J. Am. Chem. Soc.* **2013**, *135*, 8432−8435.

(33) Wasylenko, D. J.; Palmer, R. D.; Schott, E.; Berlinguette, C. P. Interrogation of electrocatalytic water oxidation mediated by a cobalt complex. *Chem. Commun.* **2012**, *48*, 2107−2109.
(34) Wasylenko, D. J.; Ganesamoorthy, C.; Borau-Garcia, J.; Berlinguette, C. P. Electrochemical evidence for catalyticwater oxidation mediated by a high-valent cobalt complex. *Chem. Commun.* **2011**, *47*, 4249−4251.
(35) Siewert, I.; Gałęzowska, J. Cobalt catalyst with a proton-responsive ligand for water oxidation. *Chem. − Eur. J.* **2015**, *21*, 2780−2784.
(36) Nakazono, T.; Parent, A. R.; Sakai, K. Cobalt porphyrins as homogeneous catalysts for water oxidation. *Chem. Commun.* **2013**, *49*, 6325−6327.
(37) Younus, H. A.; Ahmad, N.; Chughtai, A. H.; Vandichel, M.; Busch, M.; Van Hecke, K.; Yusubov, M.; Song, S.; Verpoort, F. A robust molecular catalyst generated in situ for photo- and electrochemical water oxidation. *ChemSusChem* **2017**, *10*, 862−875.
(38) Das, D.; Pattanayak, S.; Singh, K. K.; Garai, B.; Sen Gupta, S. Electrocatalytic water oxidation by a molecular cobalt complex through a high valent cobalt oxo intermediate. *Chem. Commun.* **2016**, *52*, 11787−11790.
(39) Mondal, B.; Chattopadhyay, S.; Dey, S.; Mahammed, A.; Mittra, K.; Rana, A.; Gross, Z.; Dey, A. Elucidation of factors that govern the $2e^-/2H^+$ vs $4e^-/4H^+$ selectivity of water oxidation by a cobalt corrole. *J. Am. Chem. Soc.* **2020**, *142*, 21040−21049.
(40) Sinha, W.; Mizrahi, A.; Mahammed, A.; Tumanskii, B.; Gross, Z. Reactive intermediates involved in cobalt corrole catalyzed water oxidation (and oxygen reduction). *Inorg. Chem.* **2018**, *57*, 478−485.
(41) Sun, H.; Han, Y.; Lei, H.; Chen, M.; Cao, R. Cobalt corroles with phosphonic acid pendants as catalysts for oxygen and hydrogen evolution from neutral aqueous solution. *Chem. Commun.* **2017**, *53*, 6195−6198.
(42) Xu, L.; Lei, H.; Zhang, Z.; Yao, Z.; Li, J.; Yu, Z.; Cao, R. The effect of the trans axial ligand of cobalt corroles on water oxidation activity in neutral aqueous solutions. *Phys. Chem. Chem. Phys.* **2017**, *19*, 9755−9761.
(43) Safdari, R.; Mohammadi, M. R.; Hołyńska, M.; Chernev, P.; Dau, H.; Najafpour, M. M. A mononuclear cobalt complex for water oxidation: new controversies and puzzles. *Dalton Trans.* **2018**, *47*, 16668−16673.
(44) Du, H.-Y.; Chen, S.-C.; Su, X.-J.; Jiao, L.; Zhang, M.-T. Redox-active ligand assisted multielectron catalysis: a Case of coIII complex as water oxidation catalyst. *J. Am. Chem. Soc.* **2018**, *140*, 1557−1565.
(45) Biswas, S.; Bose, S.; Debgupta, J.; Das, P.; Biswas, A. N. Redox-active ligand assisted electrocatalytic water oxidation by a mononuclear cobalt complex. *Dalton Trans.* **2020**, *49*, 7155−7165.
(46) Schley, N. D.; Blakemore, J. D.; Subbaiyan, N. K.; Incarvito, C. D.; D'Souza, F.; Crabtree, R. H.; Brudvig, G. W. Distinguishing homogeneous from heterogeneous catalysis in electrode-driven water oxidation with molecular iridium complexes. *J. Am. Chem. Soc.* **2011**, *133*, 10473−10481.
(47) Garrido-Barros, P.; Matheu, R.; Gimbert-Suriñach, C.; Llobet, A. Electronic, mechanistic, and structural factors that influence the performance of molecular water oxidation catalysts anchored on electrode surfaces. *Curr. Opin. Electrochem.* **2019**, *15*, 140−147.
(48) Bairagya, M. D.; Bujol, R. J.; Elgrishi, N. Fighting deactivation: classical and emerging strategies for efficient stabilization of molecular electrocatalysts. *Chem. − Eur. J.* **2020**, *26*, 3991−4000.
(49) Bullock, R. M.; Das, A. K.; Appel, A. M. Surface immobilization of molecular electrocatalysts for energy conversion. *Chem. − Eur. J.* **2017**, *23*, 7626−7641.
(50) Ding, Y.; Klyushin, A.; Huang, X.; Jones, T.; Teschner, D.; Girgsdies, F.; Rodenas, T.; Schlögl, R.; Heumann, S. Cobalt-bridged ionic liquid polymer on a carbon nanotube for enhanced oxygen evolution reaction activity. *Angew. Chem., Int. Ed.* **2018**, *57*, 3514−3518.
(51) Geer, A. M.; Liu, C.; Musgrave, C. B., III; Webber, C.; Johnson, G.; Zhou, H.; Sun, C.-J.; Dickie, D. A.; Goddard, W. A., III; Zhang, S.; Gunnoe, T. B. Noncovalent immobilization of pentamethylcyclopentadienyl iridium complexes on ordered mesoporous carbon for electrocatalytic water oxidation. *Small Sci.* **2021**, *1*, 2100037.
(52) Sheridan, M. V.; Sherman, B. D.; Xie, Y.; Wang, Y. Heterogeneous water oxidation catalysts for molecular anodes and photoanodes. *Sol. RRL* **2021**, *5*, 2000565.
(53) Baydoun, H.; Burdick, J.; Thapa, B.; Wickramasinghe, L.; Li, D.; Niklas, J.; Poluektov, O. G.; Schlegel, H. B.; Verani, C. N. Immobilization of an amphiphilic molecular cobalt catalyst on carbon black for ligand-assisted water oxidation. *Inorg. Chem.* **2018**, *57*, 9748−9756.
(54) Gonawala, S.; Baydoun, H.; Wickramasinghe, L.; Verani, C. N. Efficient water oxidation with electromodified Langmuir−Blodgett films of procatalytic $[Co^{III}(N_2O_3)]$ metallosurfactants on electrodes. *Chem. Commun.* **2016**, *52*, 8440−8443.
(55) Morlanés, N.; Takanabe, K.; Rodionov, V. Simultaneous reduction of CO_2 and splitting of H_2O by a single immobilized cobalt phthalocyanine electrocatalyst. *ACS Catal.* **2016**, *6*, 3092−3095.
(56) Morlanés, N.; Joya, K. S.; Takanabe, K.; Rodionov, V. Perfluorinated cobalt phthalocyanine effectively catalyzes water electrooxidation. *Eur. J. Inorg. Chem.* **2015**, *2015*, 49−52.
(57) Li, C.; Huang, T.; Huang, Z.; Sun, J.; Zong, C.; Yang, J.; Deng, W.; Dai, F. A sulfonated cobalt phthalocyanine/carbon nanotube hybrid as a bifunctional oxygen electrocatalyst. *Dalton Trans.* **2019**, *48*, 17258−17265.
(58) Li, T.-T.; Qian, J.; Zhou, Q.; Lin, J.-L.; Zheng, Y.-Q. A pyrene-modified cobalt salophen complex immobilized on multiwalled carbon nanotubes acting as a precursor for efficient electrocatalytic water oxidation. *Dalton Trans.* **2017**, *46*, 13020−13026.
(59) Li, H.; Li, X.; Lei, H.; Zhou, G.; Zhang, W.; Cao, R. Convenient immobilization of cobalt corroles on carbon nanotubes through covalent bonds for electrocatalytic hydrogen and oxygen evolution reactions. *ChemSusChem* **2019**, *12*, 801−806.
(60) O'Reilly, M. E.; Fu, R.; Nielsen, R. J.; Sabat, M.; Goddard, W. A.; Gunnoe, T. B. Long-range C−H bond activation by Rh^{III}-carboxylates. *J. Am. Chem. Soc.* **2014**, *136*, 14690−14693.
(61) Fu, R.; O'Reilly, M. E.; Nielsen, R. J.; Goddard, W. A., III; Gunnoe, T. B. Rhodium Bis(quinolinyl)benzene complexes for methane activation and functionalization. *Chem. − Eur. J.* **2015**, *21*, 1286−1293.
(62) O'Reilly, M. E.; Johnson, S. I.; Nielsen, R. J.; Goddard, W. A., III; Gunnoe, T. B. Transition-metal-mediated nucleophilic aromatic substitution with acids. *Organometallics* **2016**, *35*, 2053−2056.
(63) Chen, J.; Nielsen, R. J.; Goddard, W. A.; McKeown, B. A.; Dickie, D. A.; Gunnoe, T. B. Catalytic synthesis of superlinear alkenyl arenes using a Rh(I) catalyst supported by a "capping arene" ligand: access to aerobic catalysis. *J. Am. Chem. Soc.* **2018**, *140*, 17007−17018.
(64) Gu, S.; Chen, J.; Musgrave, C. B.; Gehman, Z. M.; Habgood, L. G.; Jia, X.; Dickie, D. A.; Goddard, W. A.; Gunnoe, T. B. Functionalization of RhIII−Me bonds: use of "capping arene" ligands to facilitate Me−X reductive elimination. *Organometallics* **2021**, *40*, 1889−1906.
(65) Gu, S.; Musgrave, C. B.; Gehman, Z. M.; Zhang, K.; Dickie, D. A.; Goddard, W. A.; Gunnoe, T. B. Rhodium and iridium complexes bearing "capping arene" ligands: synthesis and characterization. *Organometallics* **2021**, *40*, 2808−2825.
(66) Queyriaux, N. Redox-active ligands in electroassisted catalytic H^+ and CO_2 reductions: benefits and risks. *ACS Catal.* **2021**, *11*, 4024−4035.
(67) Addison, A. W.; Rao, T. N.; Reedijk, J.; van Rijn, J.; Verschoor, G. C. Synthesis, structure, and spectroscopic properties of copper(II) compounds containing nitrogen−sulphur donor ligands; the crystal and molecular structure of aqua[1,7-bis(N-methylbenzimidazol-2′-yl)-2,6-dithiaheptane]copper(II) perchlorate. *J. Chem. Soc., Dalton Trans.* **1984**, 1349−1356.
(68) Jiao, Y.; Han, D.; Liu, L.; Ji, L.; Guo, G.; Hu, J.; Yang, D.; Dong, A. Highly ordered mesoporous few-layer graphene fframeworks enabled by Fe_3O_4 nanocrystal superlattices. *Angew. Chem., Int. Ed.* **2015**, *54*, 5727−5731.

https://doi.org/10.1021/acscatal.1c04617
ACS Catal. 2021, 11, 15068−15082

(69) He, Y.; Han, X.-P.; Rao, D.-W.; Zhang, Y.-D.; Zhao, J.; Zhong, C.; Hu, W.-B.; Wei, W.-F.; Deng, Y.-D. Charge redistribution of Co on cobalt (II) oxide surface for enhanced oxygen evolution electrocatalysis. *Nano Energy* **2019**, *61*, 267−274.
(70) Chou, N. H.; Ross, P. N.; Bell, A. T.; Tilley, T. D. Comparison of cobalt-based nanoparticles as electrocatalysts for water oxidation. *ChemSusChem* **2011**, *4*, 1566−1569.
(71) Ping, Y.; Nielsen, R. J.; Goddard, W. A. The reaction mechanism with free energy barriers at constant potentials for the oxygen evolution reaction at the IrO_2 (110) surface. *J. Am. Chem. Soc.* **2017**, *139*, 149−155.
(72) Xiao, H.; Shin, H.; Goddard, W. A. Synergy between Fe and Ni in the optimal performance of (Ni,Fe)OOH catalysts for the oxygen evolution reaction. *Proc. Natl. Acad. Sci. U. S. A.* **2018**, *115*, 5872.
(73) Crandell, D. W.; Ghosh, S.; Berlinguette, C. P.; Baik, M.-H. How a $[Co^{IV}O]^{2+}$ fragment oxidizes water: involvement of a biradicaloid $[Co^{II}-(\cdot O\cdot)]^{2+}$ species in forming the O-O bond. *ChemSusChem* **2015**, *8*, 844−852.
(74) Funes-Ardoiz, I.; Garrido-Barros, P.; Llobet, A.; Maseras, F. Single electron transfer steps in water oxidation catalysis. redefining the mechanistic scenario. *ACS Catal.* **2017**, *7*, 1712−1719.
(75) Mao, Q.-Y.; Pang, Y.-J.; Li, X.-C.; Chen, G.-J.; Tan, H.-W. Theoretical study of the mechanisms of two copper water oxidation electrocatalysts with bipyridine ligands. *ACS Catal.* **2019**, *9*, 8798−8809.
(76) Zhao, S.-B.; Song, D.; Jia, W.-L.; Wang, S. Regioselective C−H activation of toluene with a 1,2-Bis(N-7-azaindolyl)benzene platinum-(II) complex. *Organometallics* **2005**, *24*, 3290−3296.
(77) Ravel, B.; Newville, M. ATHENA, ARTEMIS, HEPHAESTUS: data analysis for X-ray absorption spectroscopy using IFEFFIT. *J. Synchrotron Radiat.* **2005**, *12*, 537−541.
(78) Bochevarov, A. D.; Harder, E.; Hughes, T. F.; Greenwood, J. R.; Braden, D. A.; Philipp, D. M.; Rinaldo, D.; Halls, M. D.; Zhang, J.; Friesner, R. A. Jaguar: A high-performance quantum chemistry software program with strengths in life and materials sciences. *Int. J. Quantum Chem.* **2013**, *113*, 2110−2142.
(79) Becke, A. D. Density-functional thermochemistry. III. The role of exact exchange. *J. Chem. Phys.* **1993**, *98*, 5648−5652.
(80) Grimme, S.; Antony, J.; Ehrlich, S.; Krieg, H. A consistent and accurate ab initio parametrization of density functional dispersion correction (DFT-D) for the 94 elements H-Pu. *J. Chem. Phys.* **2010**, *132*, 154104.
(81) Roy, L. E.; Hay, P. J.; Martin, R. L. Revised basis sets for the LANL effective core potentials. *J. Chem. Theory Comput.* **2008**, *4*, 1029−1031.
(82) Kahn, L. R.; Goddard, W. A. Ab initio effective potentials for use in molecular calculations. *J. Chem. Phys.* **1972**, *56*, 2685−2701.
(83) Zhao, Y.; Truhlar, D. G. The M06 suite of density functionals for main group thermochemistry, thermochemical kinetics, noncovalent interactions, excited states, and transition elements: two new functionals and systematic testing of four M06-class functionals and 12 other functionals. *Theor. Chem. Acc.* **2008**, *120*, 215−241.
(84) Friedrichs, M.; Zhou, R.; Edinger, S. R.; Friesner, R. A. Poisson−Boltzmann analytical gradients for molecular modeling calculations. *J. Phys. Chem. B* **1999**, *103*, 3057−3061.

https://doi.org/10.1021/acscatal.1c04617
ACS Catal. 2021, 11, 15068−15082